Ce- and Ni-codoped Double $PrBaMn_2O_5$ Perovskite as a New Ceramic SOFC Anode

Praveen B. Managutti,[a] Yeting Wen,[b] T.C. Hansen,[c] Vincent Dorcet,[d] Serge Paofai,[d] Pascal Briois,[e] Kevin Huang,[b *] and Mona Bahout [d*]

[a] Chemical Crystallography Laboratory, Khalifa University of Science and Technology, Abu Dhabi, P.O. Box 127788, United Arab Emirates

[b] Department of Mechanical Engineering, University of South Carolina, Columbia, SC, 29208, USA

[c] Institut Laue-Langevin, 71 avenue des Martyrs CS 20156, 38042 Grenoble Cedex 9, France

[d] Univ Rennes, CNRS, ISCR (Institut des Sciences Chimiques de Rennes) - UMR 6226, F-35000 Rennes, France

[e] FEMTO-ST Institute (UMR CNRS 6174), Université Bourgogne Franche-Comté, UTBM, F-25200 Montbéliard Cedex, France

Abstract

The study investigates the introduction of cerium, either alone or in combination with nickel, into the $PrBaMn_2O_{5+\delta}$ (PBM) structure, a layered double perovskite, for potential use as SOFC anode. Single-phase $Pr_{1-x}Ce_xBaMn_2O_{5+\delta}$ compositions with x = 0.05 (PrCe5) and 0.1 (PrCe10) were synthesized. Additionally, a Ni-doped composition, $Pr_{0.95}Ce_{0.05}BaMn_{1.9}Ni_{0.1}O_{5+\delta}$ (PrCe5Ni) composition was created and subjected to H_2 treatment to exsolve Ni nanoparticles. All the materials showed remarkable stability in both reducing and oxidizing conditions, indicating their viability for prolonged SOFC applications. The thermal expansion coefficient (TEC) of PrCe5 composition at ~ 13.8×10^{-6} K^{-1}, as determined by *in-situ* neutron diffraction, shows a notable improvement over the higher TEC of 16.8×10^{-6} K^{-1} of the Ce-free composition and matches the TECs of widely-used SOFC electrolytes. The application of a 3.5 µm GDC

buffer layer by physical vapor deposition (PVD has proven effective to prevent the chemical reactions between PBM-based anodes and YSZ electrolyte, a concern identified by *in-situ* neutron diffraction at temperatures below the SOFC processing threshold. Electrochemical impedance spectroscopy (EIS) data collected over 220 h in an H_2-3% H_2O environment at 750 °C indicate that this thickness yields the lowest area-specific resistance (ASR) of the electrode with the best stability at a degradation rate of 0.002 Ω cm^2/h .This performance is superior to thinner (1μm) or thicker (8μm) GDC layers, which showed a higher degradation rate of 0.15-0.2 Ω cm^2/h. Cerium doping at 5 at. % in PrCe5 anode leads to better microstructural stability and less agglomeration compared to PBM under H_2 environments, implying enhanced long-term performance and durability by Ce doping. Additionally, PrCe5 demonstrates no Ba diffusion, contrary to PBM, further suggesting improved stability and effectiveness of Ce-doping in maintaining electrode integrity over time. By integrating nickel into PrCe5, the ASR is nearly halved from 0.9 to 0.5 Ω cm^2 at 750 °C, placing it within the ideal range of 0.1 - 0.5 Ω cm^2 for SOFC anodes at this operating temperature. The marked reduction in ASR and TEC alignment with standard SOFC electrolytes suggests that PrCe5Ni is a promising anode, with potential for further compositional and microstructural optimizations to advance SOFC technology.

Keywords: SOFC, H_2 fuel, layered perovskite manganites, Ce-doping, *in situ* neutron diffraction, Ni-exsolution, GDC buffer layer thickness, Ba diffusion, electrochemical impedance spectroscopy.

Introduction

Solid Oxide Fuel Cells (SOFCs) represent a cutting-edge technology with great potential for the efficient and eco-friendly generation of power from hydrogen.[1-7] However, current SOFCs suffer from various obstacles limiting their market entry. Challenges related to the anode are prominent among these issues: severe reducing environment and high temperature. During operation, it must remain thermally stable and maintain redox stability to avoid cracking and mechanical compatibility with the electrolyte to prevent delamination. Conventional nickel–yttria stabilized zirconia (Ni–YSZ) cermet anodes face issues in terms of Ni agglomeration, redox instability due to Ni reoxidation,[8,9] and long-term deactivation caused by sulfur poisoning and coking when used with hydrocarbon fuels.[10-12] Mixed Ionic and Electron Conducting (MIEC) perovskite oxides have been considered as alternatives for Ni-based cermets to mitigate the aforementioned problems,[6] but their electrochemical activity is insufficient. It is well known that cerium, owing to its variable oxidation states (Ce^{3+} and Ce^{4+}), can contribute to oxygen ion conductivity and electrocatalytic activity important for the anodic and cathodic reactions in SOFCs.[13] For instance, substitution of 10 at. % of cerium at the A-site of $La_{0.75}Sr_{0.25}Cr_{0.5}Mn_{0.5}O_3$ has been shown to enhance SOFC's anodic performances under H_2 or CH_4.[14] Likewise, the Ce-doped anode materials $Ce_xLa_{0.75-x}Sr_{0.25}Cr_{0.5}Mn_{0.5}O_3$,[14] $Ce_xSr_{1-x}MnO_3$,[15] $(Pr,Ce)MnO_3$,[16] $La_{0.3}Ce_{0.1}Sr_{0.5}Ba_{0.1}TiO_{3-\delta}$,[17] and $La_{0.23}Ce_{0.1}Sr_{0.67}TiO_{3-\delta}$[18] have also been reported with enhanced electrooxidation kinetics in comparison with Ce-free compositions. Finally, infiltration of samarium-doped ceria (SDC) in combination with NiO into $La_{0.6}Sr_{1.4}MnO_{4+\delta}$ significantly enhanced the electrochemical activity for H_2 and CH_4 fuels oxidation.[19] These observations underscore the significance of cerium in catalysis and electrocatalysis, related to the mixed oxidation states of $Ce^{3+/4+}$.

The double-layered perovskite manganites, such as $PrBaMn_2O_{5+\delta}$ (PBM), have recently attracted attention as potential anode materials for their robust thermal stability in reducing atmospheres. However, enhancing their electrocatalytic performance remains a challenge.[19,2] Although various transition metals, metal alloys, and metal oxides have been incorporated into PBM to boost its electrochemical capabilities,[20-23] the potential benefits of cerium inclusion have not yet been explored. This presents an untapped opportunity to further elevate the functionality of PBM-based anode materials.

This study seeks to examine the impact of cerium substitution, either alone or in conjunction with nickel, on PBM anode performance for hydrogen oxidation. The chemical reactivity between a Ce-doped PBM anode and 8YSZ electrolyte was monitored through *in situ* neutron diffraction in air up to 950 °C. To prevent chemical reactivity between the electrode and electrolyte,[24] a dense gadolinia-doped ceria (GDC) buffer layer was deposited on commercial 8YSZ disks *via* physical vapor deposition (PVD), a process that does not involve high-temperature sintering. The impact of GDC thickness on the electrochemical performance and stability in a hydrogen atmosphere (with 3% H_2O) was investigated by electrochemical impedance spectroscopy.

1. Experimental

1.1 *Synthesis and characterization*

Polycrystalline $Pr_{1-x}Ce_xBaMn_2O_{5+\delta}$ with x = 0, 5, 10, 15 % (henceforth referred to as PBM, PrCe5, PrCe10, PrCe15, respectively) and $Pr_{0.95}Ce_{0.05}BaMn_{1.9}Ni_{0.1}O_{5+\delta}$ (henceforth referred to as PrCe5Ni) were prepared by the citric acid sol gel method. Stoichiometric amounts of $Pr(NO_3)_2{\cdot}6H_2O$ (Aldrich, 99.9%), $Ce(NO_3)_2.6H_2O$ (Aldrich, 98%), $Ba(NO_3)_2$ (Aldrich, 99%), $Mn(NO_3)_2{\cdot}4H_2O$ (Aldrich, 98%), $Ni(NO_3)_2{\cdot}6H_2O$ (Aldrich, 98.5 %) were dissolved in distilled water. Ethylene glycol (EG) and citric acid (CA) were added in the molar ratio to the total metal

ions (M) CA:EG:M of 1.5: 3:1. The pH value was fixed to ~ 8 by adding ammonium hydroxide to enhance cation binding to the citrate and avoid the precipitation of individual hydroxides.[25] The solution was stirred on the hot plate until a resin formed which was subsequently calcined at *T* ~ 550 °C overnight. The solid precursors were ground, pressed in pellets (13 mm diameter, 2-3 mm thickness) and sintered under 1% H_2/N_2 at 1000 °C for 48 h except PrCe5Ni which was sintered in air at 950 °C for 24 h to incorporate nickel ions into the oxide lattice. The as-prepared sample was heated in 5% H_2/Ar at 875 °C for 42 h to exsolve the Ni particles on the oxide surface resulting in the reduced sample denoted as PrCe5Ni-H. To assess redox stability, the hydrogen-annealed samples were heated in air at 800°C, resulting in the formation of the oxidized samples labeled as PrCe5-A, PrCe10-A, and PrCe5Ni-A.

All the samples were characterized by powder X-ray diffraction (XRD) using a D8-A25-Advance (Bruker) diffractometer operating in Bragg-Brentano geometry with a Cu-$K_{\alpha 1}$ radiation equipped with a silicon strip Lynxeye detector. Structural information was obtained by Rietveld refinements using the FullProf Suite program and its graphical interface WinPLOTR.[26] The surface microstructure was examined by scanning electron microscopy (SEM) using a JEOL JSM 7100 F EDS EBSD Oxford. Transmission electron microscopy (TEM) was done using a JEOL JEM-2100 LaB_6 instrument operated at 200 kV equipped with energy-dispersive spectroscopy (EDS) (OXFORD). A small amount of powder was added to ethanol, followed by ultrasonic mixing to achieve a particle dispersion. A few drops of the suspension were deposited on carbon-coated grids. Micrographs were digitally acquired on a 2 × 2 k charge-coupled device camera using a Gatan Imaging Filter system.

1.2 *Chemical reactivity with the YSZ electrolyte monitored by neutron diffraction.*

Redox stability and chemical reactivity were monitored by Neutron Powder Diffraction (NPD) on the high-flux two-axis D20 diffractometer at the *Institut Laue-Langevin* (ILL, Grenoble, France)[27]. The configuration replicates that outlined previously.[21,28-30] We selected a take-off angle of 90 degrees from the (115) plane of a germanium monochromator, which yielded $\lambda \sim 1.54$ Å and a resolution of $\Delta d/d \sim 2.9 \times 10^{-3}$. This setup maintains a high flux, $\sim 1.6 \times 10^{7}$ neutrons per square centimeter per second. The sample consists of a 2-gram pellet mixture of PrCe5:8YSZ in a 50:50 wt. % ratio, which is loaded into an 8 mm quartz cell. A heating and cooling cycle was performed under synthetic air, spanning a temperature range from 20 to 950 °C at a rate of 10 °C/min. Data were collected at five-minute intervals throughout this thermal cycle. Additionally, isothermal data sets were recorded over a period of 2 h both at the start and end of the cycle, as well as at the peak temperature of 950 °C. The Rietveld refinement was performed using the FullProf Suite software. Background modeling was achieved through a linear interpolation function, and the profile was fitted using the Thompson-Cox-Hastings Pseudo-Voigt function.[31] The standard deviation values were corrected according to Berar's and Lelann's. description.[32]

1.3 *Symmetrical cell fabrication*

Symmetrical cells were fabricated using commercial 230 µm-thick 8YSZ disks, each measuring 25 mm in diameter (Tosoh). To prevent ionic interdiffusion and chemical reactions, a $Ce_{0.9}Gd_{0.1}O_{1.95}$ (GDC) buffer layer was deposited on both sides of the electrolyte through physical vapor deposition.[33] The experimental setup comprises a 100-litre Alcatel SCM 650 sputtering chamber, evacuated by an integrated system that includes an XDS35i Dry Pump and a 5401CP turbo-molecular pump. This chamber is outfitted with a trio of magnetron targets,

each 200 mm in diameter, and a rotating substrate holder of 620 mm diameter, positioned parallel to the targets at an approximate distance of 110 mm. The separation between the central axis of the targets and that of the substrate holder is 170 mm. For sputter deposition, we employ a 10 at. % Gd-Ce target, powered by an Advanced Energy dual generator capable of pulsating DC. This generator facilitates control over the discharge's current, power, and voltage. The deposition process is regulated by a Plasma Emission Monitoring system, which operates on a closed-loop control mechanism and utilizes optical emission spectroscopy to monitor plasma emissions. For this study, we have set the discharge current at a steady 2.5 A, while maintaining the total pressure at approximately 0.2 Pa. Additional methodological details have been documented elsewhere.[34] Various thicknesses of the GDC layer, ranging from 1 to 13 µm, were investigated. The anode slurry, consisting of 50 wt. % electrode powder and 50 wt. % organic binder (V-006, Heraeus), was screen-printed on both sides of the GDC/8YSZ/GDC electrolyte and calcined in air for 2 hours at T = 1100 °C, a condition under which no reaction occurred with GDC. However, increasing the temperature to 1200 °C could potentially trigger a reaction between YSZ and GDC, potentially leading to the formation of $(Zr,Ce)O_2$ solid solutions,[24,35] which display reduced ionic conductivity. The electrode had an effective area of 1.3 cm² and an approximate thickness of 20 µm. Gold paste (C5756, Heraeus) was applied atop each electrode to improve the contact between the electrode and the current collectors by filling in any microscale gaps or irregularities on the surface, which might otherwise increase contact resistance. Silver mesh and silver wire served as the current collectors. Subsequently, the components were heated in air at 700 ºC for 2h to ensure proper attaching.

Prior to and following the EIS tests, the interfaces between the electrode, GDC, and YSZ were examined using a Scanning Transmission Electron Microscope (STEM, Hitachi HD-2000) and energy dispersive X-ray spectroscopy (EDS SDD, X-Max 80 mm^2 Oxford Instruments AZtecEnergy, England) to evaluate the microstructural integrity and detect any changes at the

nanoscale level. Occasionally, the surface of the electrodes underwent XRD analysis (Rigaku MiniFlex II device, utilizing Cu Kα radiation) before and after conducting the electrochemical tests. This analysis is aimed to identify any crystalline phase changes or reactions that may have occurred during electrode processing or testing. The XRD patterns were acquired over a 2θ range of 10- 80°, with a step size of 0.02 ° and a scanning rate of 2 ° min^{-1}.

1.4 *Electrochemical Measurements*

The EIS spectra were recorded using a Solartron 1470/1455B multi-channel electrochemical station, with frequency range of 10^5 Hz-10 mHz and an AC signal amplitude of 10 mV under open-circuit voltage (OCV) conditions. These spectra were analyzed using the Zview software. All impedance data were normalized to the electrode area (1.3 cm^2) and were fitted using an equivalent circuit that included inductance to account for the electrical lead effects and a series resistance (R_s), primarily attributed to the electrolyte conductivity. For better comparison of the electrode polarization resistances, all EIS data were plotted in the quadrant of positive -Z'/Z' values. The measurements were conducted in temperature range of 750-450 °C in a wet H_2-3% H_2O environment, with a flow rate of 100 mL min^{1}. The measurements started once the system achieved stability at 750 °C.

3. Results and discussion

3.1 *Structural analysis*

Figure 1 shows X-ray diffraction patterns from as-prepared PBM, PrCe5, PrCe10, and PrCe15. The main diffraction peaks corresponded closely with the predicted patterns for $PrBaMn_2O_6$ (JCPDS # 01-076-6163). In PrCe15, the presence of a peak at approximately 2θ = 28°, which can be attributed to the (111) plane of CeO_2 (JCPDS # 34.0394) indicates that the solubility limit has likely been surpassed by the 15 mol % concentration of Ce. The increase in lattice

parameters, as evidenced by Figure S1 & Table S1, suggests that Ce^{3+} ions have substituted Pr^{3+} ions. This assertion is corroborated by the ionic radii of the involved ions: Ce^{3+} has a larger ionic radius (~1.143 Å) in an eight-fold coordination than Pr^{3+} (1.126 Å), whereas the ionic radius of Ce^{4+} is smaller (0.97 Å).[36]

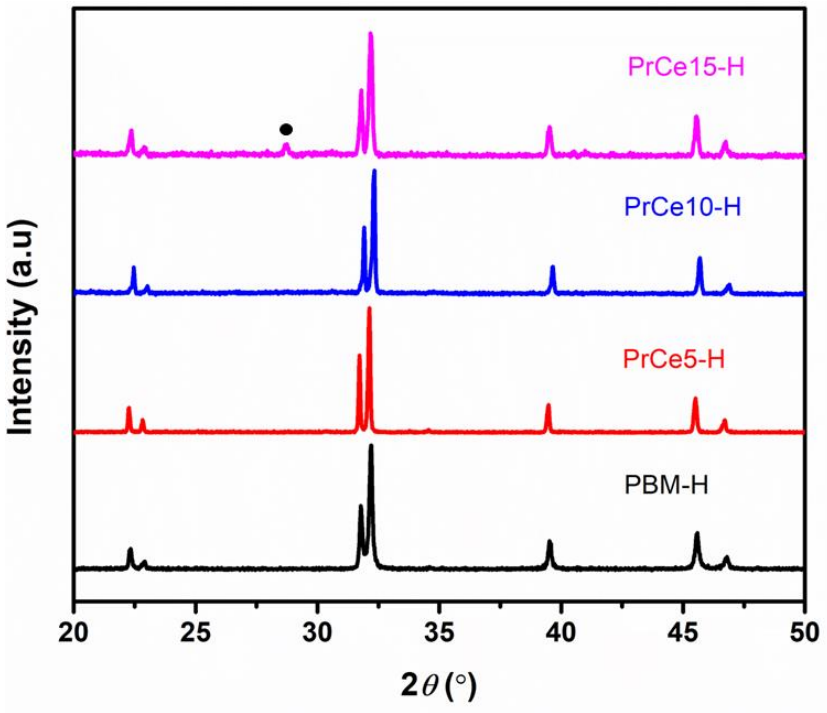

Figure 1. XRD patterns of as-prepared layered double perovskites. The peak from CeO_2 (●) in PrCe15-H is highlighted.

From the multiphase Rietveld analysis, the CeO_2 phase in PrCe15 was estimated at 2.4 (2) wt.%, signifying a solubility limit of 8.6 cerium at. %. Given that concentration falls short of the intended 10 at. % in the PrCe10 composition, our investigation will be more effectively concentrated on the PrCe5 and PrCe5Ni compositions, compared with the Ce-free PBM one.

The thermal stability of PBM and PrCe5 was studied in air at 800 °C to check if they can withstand typical SOFC operation environments. As shown in Figure S2, the XRDs of the oxidized samples, referred to as PrCe5-A and PBM-A, are inherent to single-phase materials that share the same *P*4/*mmm* structure of the as-prepared compositions validating their potential for long-term use in SOFC applications. Both a and c lattice parameters have decreased (Table

S2) due to the change in manganese oxidation state from $Mn^{+2.5}$ to $Mn^{+3.5}$, following the insertion of oxygen ions into the (Pr/Ce)O layer.[37]

3.2 *PrCe5Ni sample*

To synthesize the $Pr_{0.9}Ce_{0.05}BaMn_{1.9}Ni_{0.1}O_{5+\delta}$ composition (referred to as PrCe5Ni) and to ensure the incorporation of nickel ions into the oxide lattice, the powder mixture was annealed in air at 950 °C for 12 hours. The XRD pattern presented in **Figure 2** indicates the presence of both orthorhombic and hexagonal perovskite phases, which agrees with previous reports on related compositions.[21]

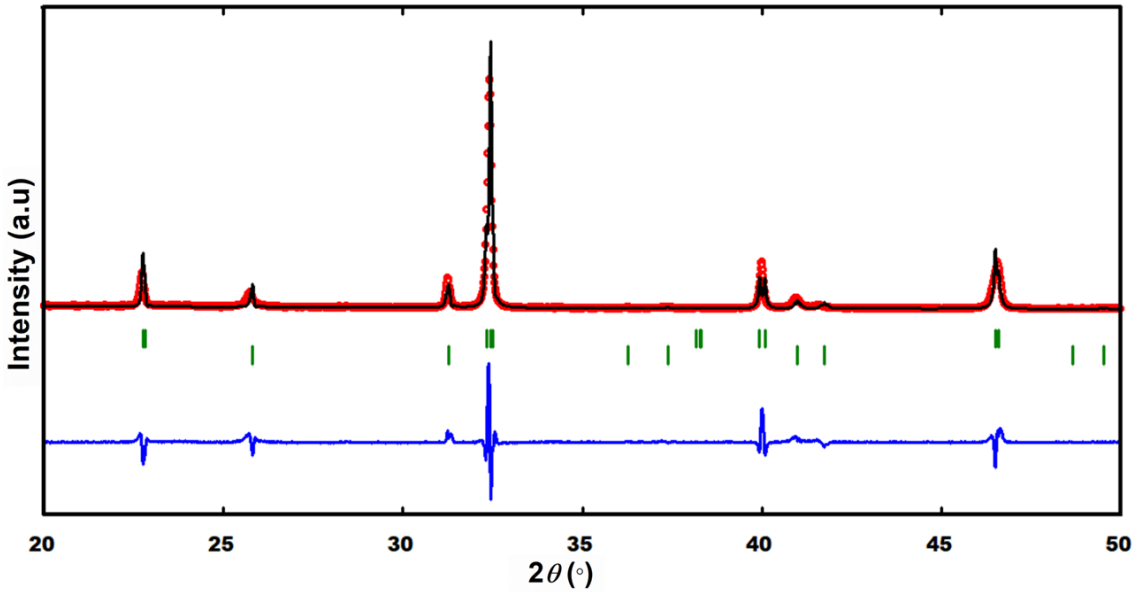

Figure 2. Rietveld refinement for as-prepared PrCe5Ni. Tick marks refer to (upper) (Pr,Ba)$MnO_{3-\delta}$, S.G. *Ibmm*, and (lower) 2H-$BaMnO_{3-\delta}$, S.G. *P*6_3/*mmc*) perovskites.

To exsolve the nickel particles, the PrCe5Ni sample underwent a heat treatment in a 5% H_2/N_2 atmosphere at T ~ 850 °C. This elevated temperature removed oxygen from the PrOx layer resulting in a structural reconstruction to a layered double perovskite (a = 3.9748 (1) Å, c = 7.7651 (2) Å) coupled with the complete exsolution of nickel (~1.3 wt.%), as confirmed by Rietveld analysis. The XRD pattern in Figure 3 revealed trace amounts of Pr_2O_3 and $PrMnO_3$, each less than 1 wt.%, were detected.

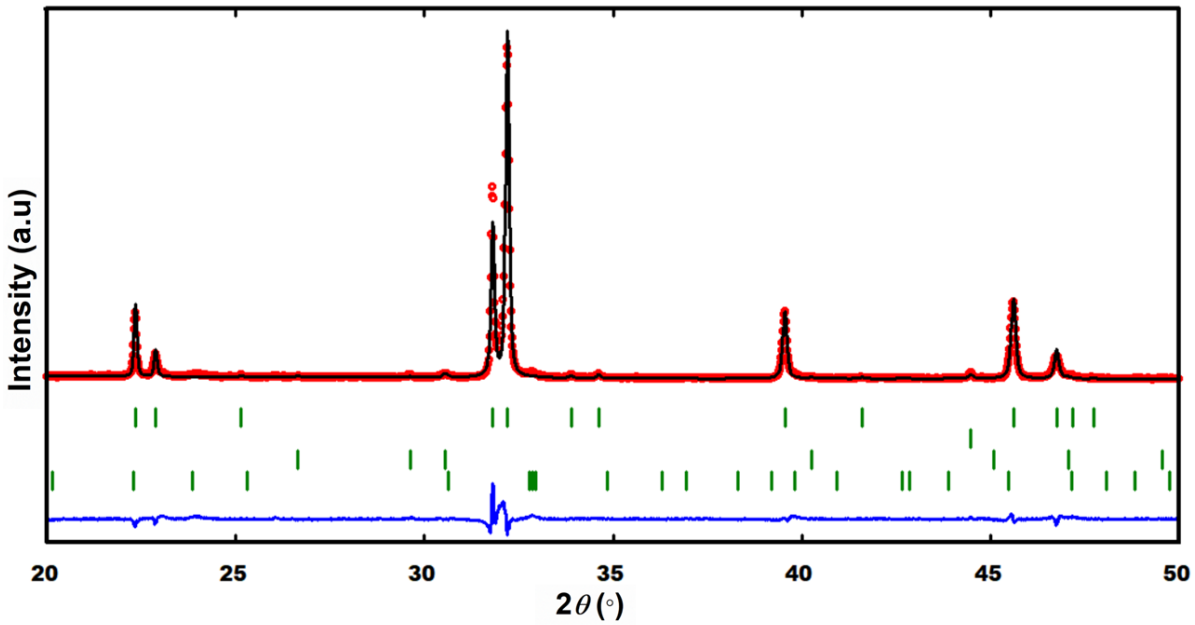

Figure 3. Rietveld refinement for PrCe5Ni after hydrogen reduction at *T* = 875 °C. Tick marks refer to (upper row) PrCe5, (second row) Ni metal, (third row) Pr_2O_3, and (lower row) $PrMnO_3$.

To evaluate the reversibility of nickel exsolution and dissolution, the PrCe5Ni sample was heated in air at a temperature of ~ 800 °C overnight. The XRD pattern in Figure 4 indicates that the Pr_2O_3 and $PrMnO_3$ impurity phases as well as most of the nickel dissolve into the layered perovskite structure. Nevertheless, small amounts of NiO (~ 0.30 wt.%, representing ~ 20 % of the Ni content) and CeO_2 (~ 0.22 wt.%) remained, which may further dissolve into the structure at higher temperatures. Given the difficulties associated with nickel insertion in layered double perovskites,[21] this significant reversibility could be advantageous for catalyst regeneration, potentially enhancing the anode longevity. Following oxidation, the cell experienced a contraction with parameters a = 3.90150 (5) Å and c = 7.7490 (1) Å, leading to a volume decrease of approximately 1.3%. While this volumetric expansion remains high, it is markedly less than the ~40% expansion seen when nickel is oxidized within a Ni-YSZ cermet.[38] The addition of a ceramic phase, such as GDC, to the electrode material could lead to a more uniform distribution of mechanical stress, thus mitigating the effects of this expansion.

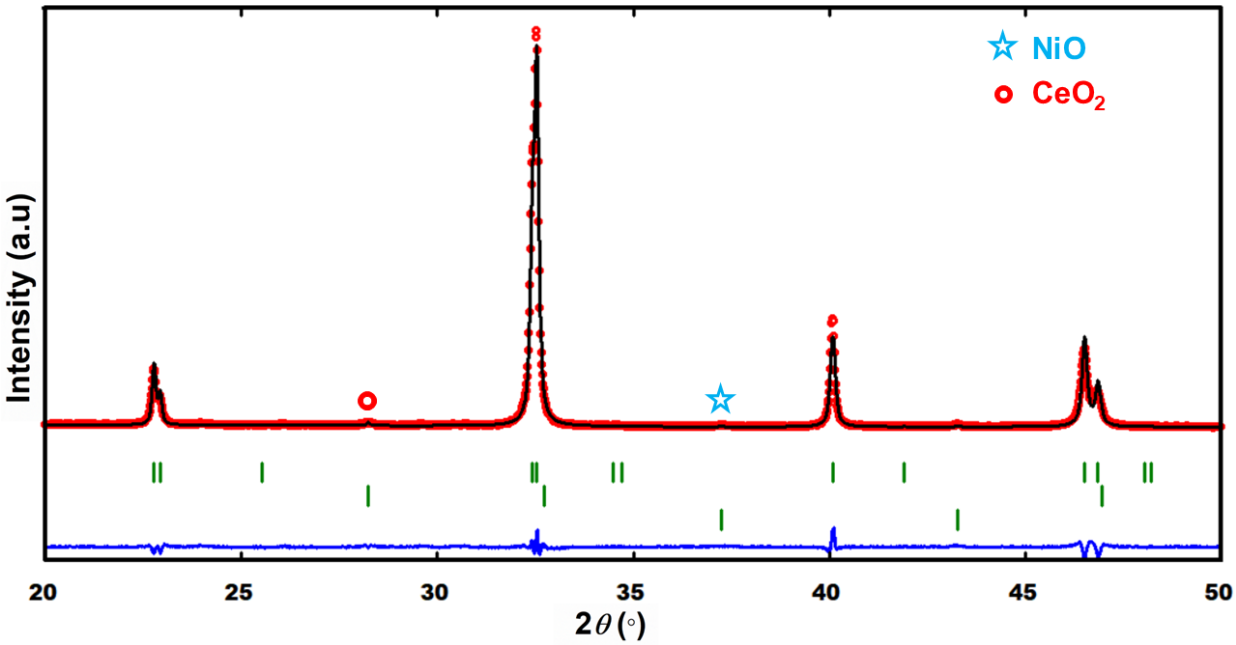

Figure 4. Observed, calculated, and different patterns for the oxidized PrCe5Ni sample.

Analysis of the surface of the as-prepared sample by scanning electron microscopy (SEM) reveals particles with irregular, rounded, granular morphology, as shown in Figure 5a. These particles exhibit some aggregation and display variable size, but predominantly fall within the nanometer scale. The surface of the reduced sample in Figure 5b has a rough texture showing a multitude of spherical or near-spherical particles uniformly distributed. Additionally, the crystal reconstruction upon reduction seems to have increased the grain size of the support. Interestingly, on the surface of the reoxidized sample in Figure 5c, the exsolved particles are no longer observed, and the grain size of the support remained consistent following oxidation.

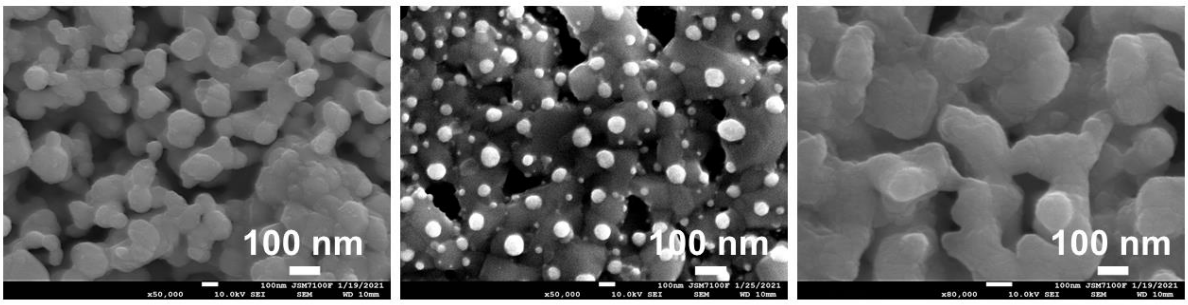

a ***b*** ***c***

Figure 5. SEM images of (a) as prepared, (b) reduced where the exsolved Ni particles appear as white spheres, and (c) oxidized PrCe5Ni samples.

A further detailed investigation was carried out using Transmission Electron Microscopy (TEM). This advanced technique revealed that the exsolved particles in PrCe5Ni are approximately 40 nm in diameter, as depicted in **Figure 6**.

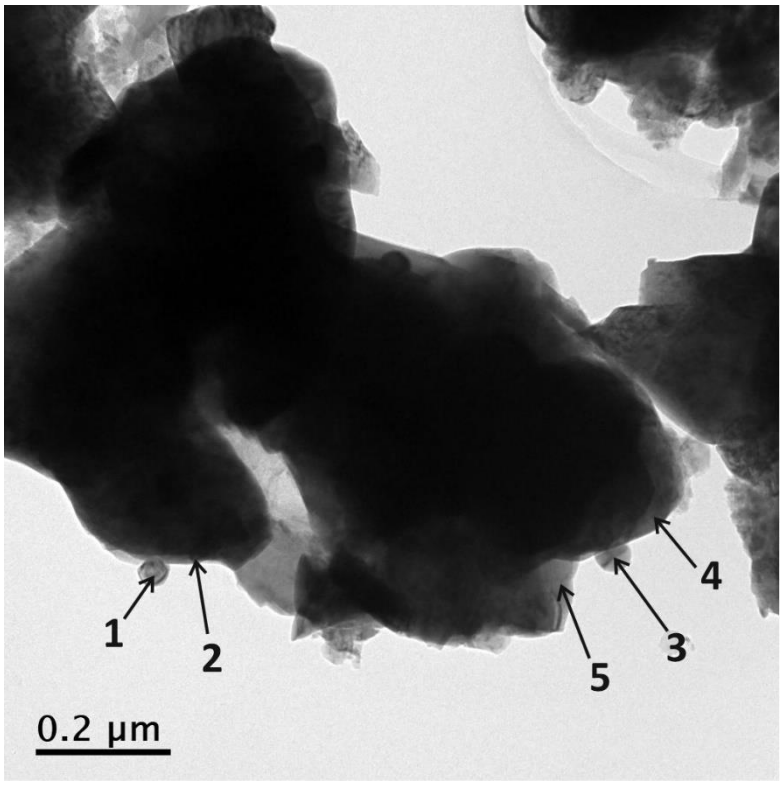

Figure 6. TEM bright field image of reduced PrCe5Ni, with corresponding EDS metal composition in at.%. Points labeled '1' and '3' indicate nickel particles, detailed in Table S2.

Table 1 presents the EDS quantification of five different points. Points 1 and 3 are dominated by Ni, and contain only trace amounts of Mn, Ba, Pr and Ce, suggesting that they are nickel particles. Points 2, 4, and 5 show a similar composition with a high presence of Mn, Ba, and Pr, and an exceptionally low presence of Ni and Ce suggesting that these points are in the perovskite phase. The slight composition variations between these points could be due to slight changes in composition or measurement inaccuracy. The significant difference in composition between points 1 and 3 *versus* points 2, 4, and 5 indicates that the sample is a composite material corresponding to Ni catalyst nanoparticles and a perovskite ceramic anode material. It should be emphasized that EDS offers a semi-quantitative evaluation, frequently supplemented by

other methods for more accurate quantification. Typically, EDS can achieve an accuracy within a few percent for elements that are abundant in a sample. However, for elements present in smaller quantities, such as cerium with a nominal concentration of 1.25 at. % in the PrCe5Ni sample, the relative error could approach 10-20%. Therefore, the possibility that cerium underwent a similar exsolution process as observed in Ni/Ce co-doped titanates resulting in nickel particles enveloped by a CeO_2 shell cannot be definitively ruled out.[39]

Table 1: Quantitative EDS Analysis for Locations 1 to 5 as presented in Figure 7.

	Mn	Ni	Ba	Ce	Pr
1	0,73	98,79	0,39	0,02	0,06
2	44,93	0,08	27,01	1,46	26,52
3	0,96	97,67	0,57	0,12	0,68
4	43,18	0,11	27,97	1,26	27,48
5	43,31	0,04	28,10	1,84	26,71

3.3 *Chemical Reactivity with the Electrolytes*

Understanding the chemical compatibility between potential electrode and electrolyte materials is crucial in crafting advanced ceramics with superior properties. To this end, the PrCe5/GDC powder mixture underwent a heat treatment at 1200 °C for 3h. Comparative analysis of diffraction patterns, presented in Figure 7, before and after this thermal exposure reveals exclusive peaks corresponding to PrCe5 and GDC. This observation strongly indicates favorable chemical compatibility between the materials, reinforcing their potential to synergize effectively in high-temperature ceramic applications.

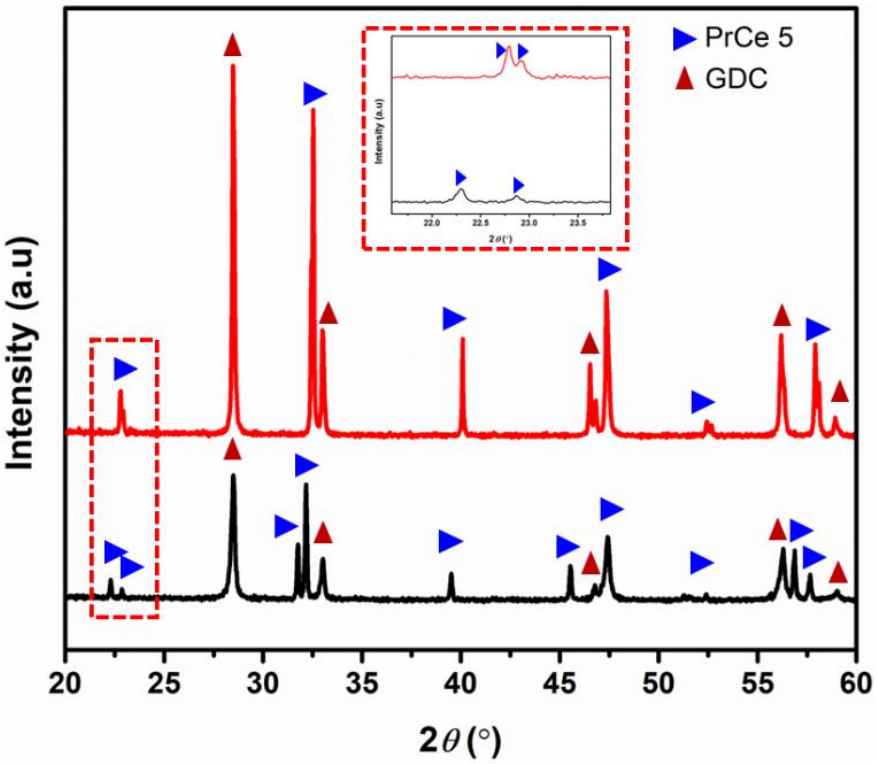

Figure 7. XRD patterns of PrCe5/GDC 50/50w/w (black) before and (red) after heating in air at 1200 °C.

Conversely, after firing the PrCe5/YSZ mixture at 1200 °C for 3 hours, new diffraction peaks at 2θ = 30° and 33° attributed to $BaZrO_3$ (JCPDS# 06-0399) was observed in the diffraction patterns as illustrated in Figure 8. This indicates the occurrence of an undesirable chemical interaction between PrCe5 and YSZ leading to the formation of an additional phase that could undermine the material's performance and stability.

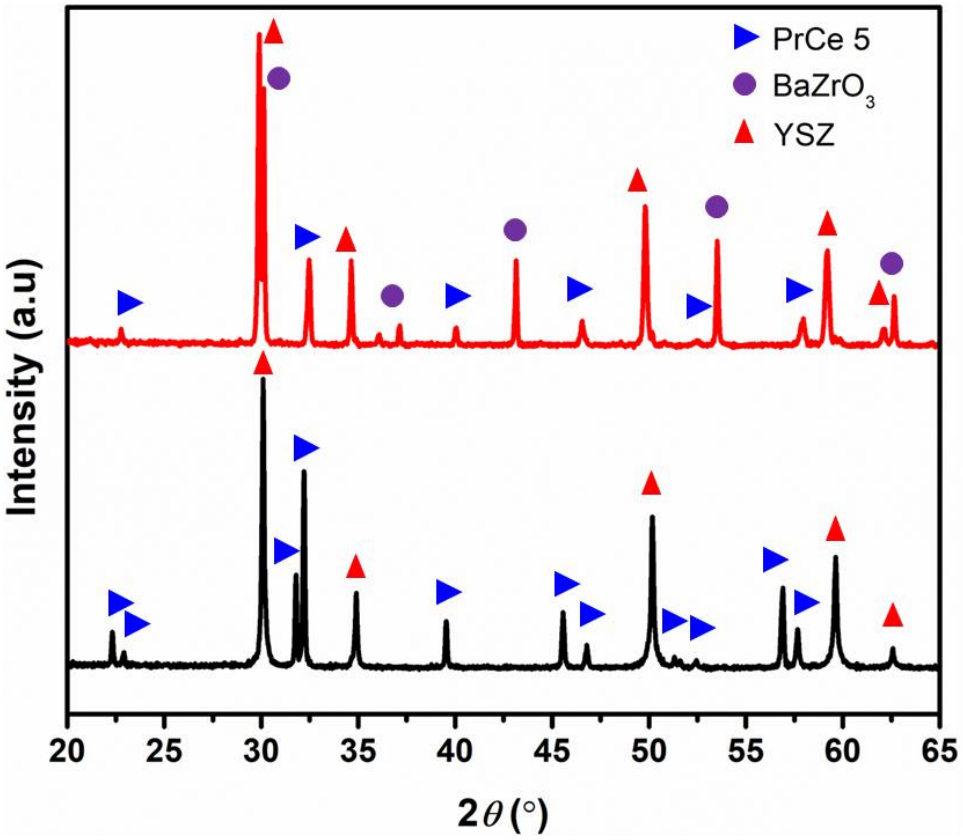

Figure 8. XRD patterns of reactivity tests for PrCe5/YSZ 50/50w/w (black) before and (red) after heating in air at 1200 °C for 3 h.

To have deeper insight into the reactivity of the PrCe5 electrode material with 8YSZ, neutron patterns were collected on a PrCe5/YSZ pellet on heating in air up to 950 °C. The structure of PrCe5 was refined in the S.G. *P*4/*mmm* consistent with the absence of Mn^{3+}/Mn^{2+} charge ordering.[40] The structure of 8YSZ was refined in the S.G. *Fm*-3*m*. The pattern obtained at T = 20 °C is displayed in Figure 9 and the structural parameters are listed in Table S3.

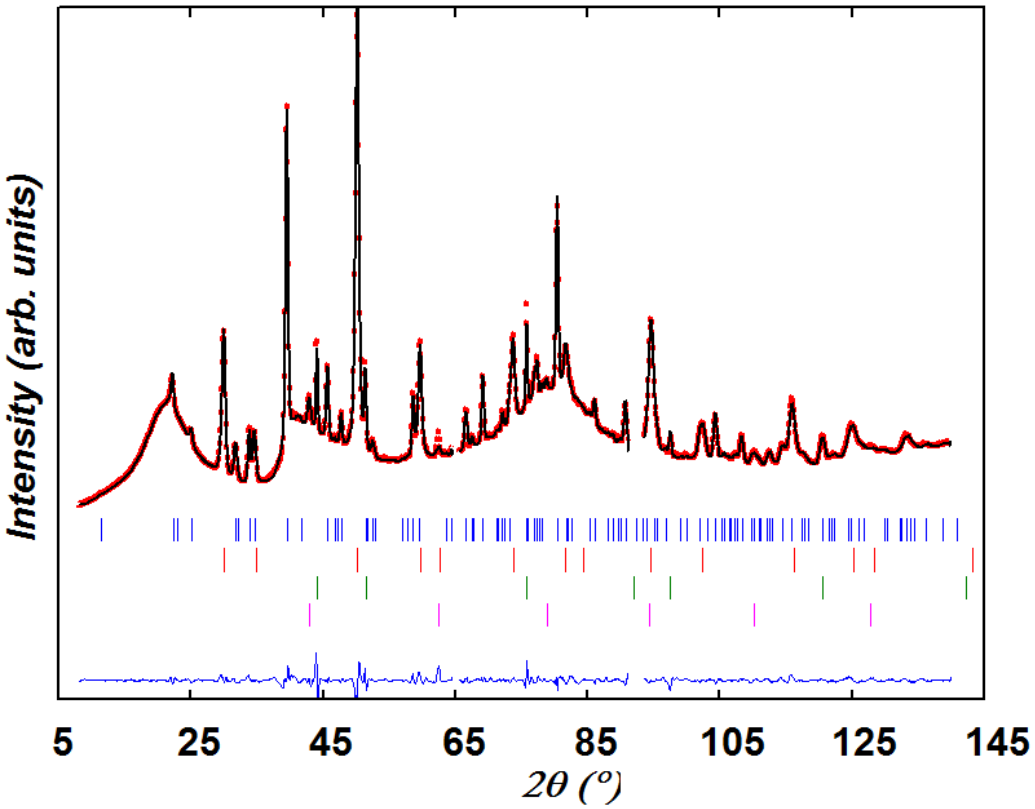

Figure 9. **Neutron Powder Diffraction (NPD) pattern of PrCe5/8YSZ composite collected at 20 °C, using a wavelength of 1.54 Å. Tick marks indicate phases from PrCe5 (first row) and YSZ (second row). The presence of the Chromel-Alumel thermocouple (S.G. Fm-3m, third row) and the vanadium heating element (S.G. *Im*-3*m*, fourth row) is also noted.**

Upon heating, oxidation of PrCe5 proceeds in the temperature range T ~ 260-315 °C as shown on Figure 10.

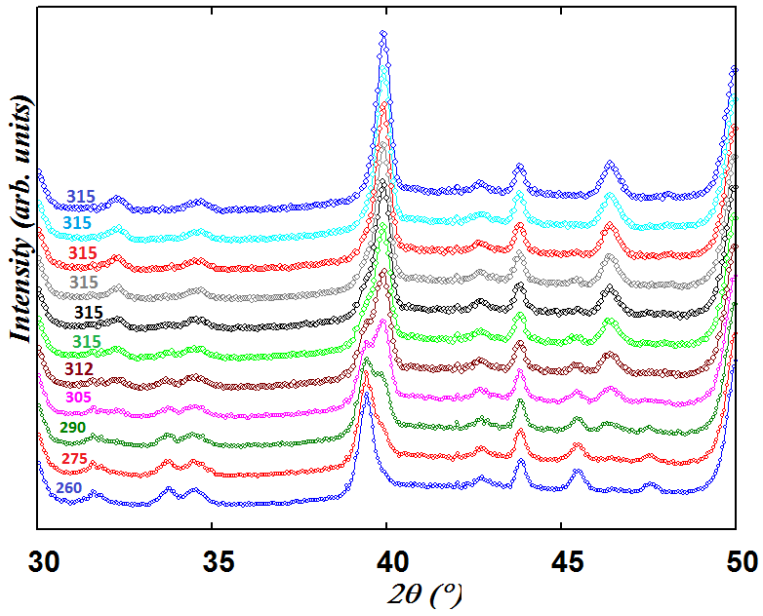

Figure 10. Neutron Powder Diffraction (NPD patterns of PrCe5/8YSZ composite collected in air within the oxidation temperature range using a wavelength of 1.54 Å. Temperature increases upwards.

A 2-phase model related to the reduced and oxidized phases was needed to fit representative data displayed in Figure 11. This is indicative of a heterogeneous reaction front within the sample, with oxidation initiating at the grain boundaries and progressing inwards. As the temperature increases, the peak intensities for the reduced phase diminish, while those corresponding to the oxidized phase become more pronounced, suggesting the conversion of Mn ions from a lower to a higher oxidation state. The reversible oxygen intercalation in PBM suggests that this electrode can repeatedly absorb and release oxygen without significant degradation. This property is highly beneficial for SOFCs as it can potentially improve their efficiency and lifespan. In addition, reversible oxygen can directly affect the oxygen ion conductivity and the overall electrochemical performance particularly during cycling conditions where oxygen levels fluctuate.

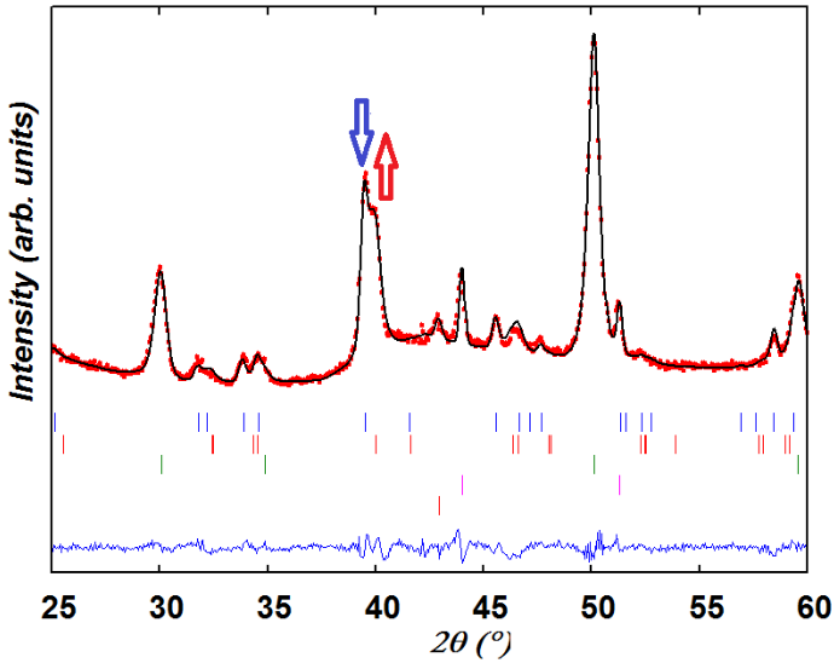

Figure 11. Rietveld analysis of the neutron data collected at 290 °C using a wavelength of 1.54 Å highlighting the progression of reduced (blue, first row) and oxidized (red, second row) PrCe5 phases. Contributions from the YSZ electrolyte (3rd row), the thermocouple (4th row) and vanadium heating element (5th row) are shown.

The subsequent analysis of PrCe5/8YSZ composite behavior by NPD data recorded at critical stages including the highest temperature reached in the neutron experiment, T = 950 °C, Figure S3, and after the thermal cycle in air in Figure 12, reveal the dominant peaks of $BaZrO_3$. These observations not only confirm the chemical reactivity between PrCe5 and 8YSZ at elevated temperatures but also parallel the reactivity with YSZ of other barium-rich electrode compositions, such as $Ba_{0.5}Sr_{0.5}Co_{0.8}Fe_{0.2}O_{3-\delta}$ (BSCF), occurring at T = 900 °C,[41] and even reported at temperatures as low as 800 °C.[42]

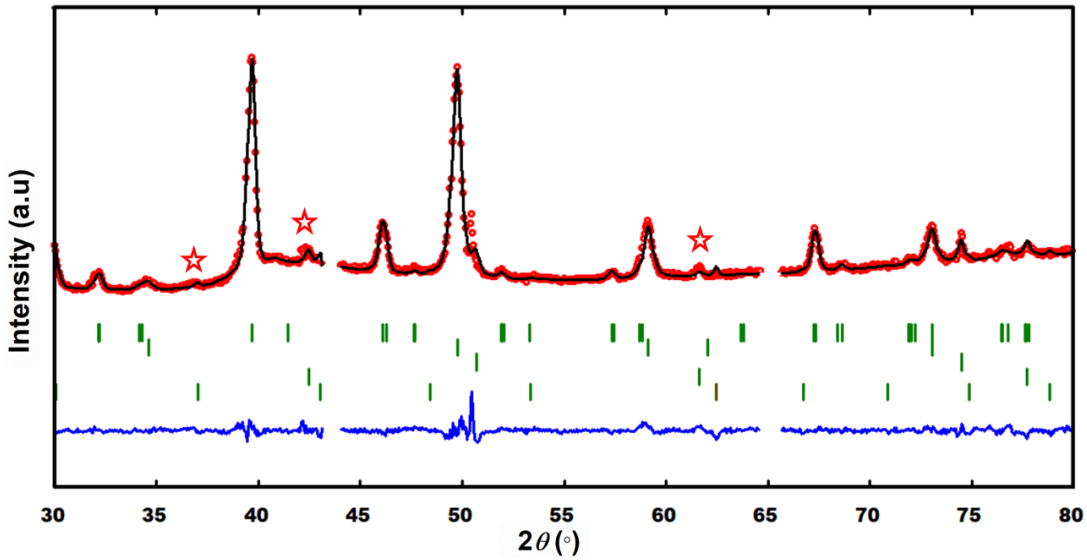

Figure 12. Neutron pattern for PrCe5/8YSZ collected at the end of the cycle in air using a wavelength of 1.54 Å. Few peaks from $BaZrO_3$ (4th row) are highlighted. The tick marks for PrCe5 (1st row), 8YSZ (2nd row), and the thermocouple material (3rd row) are delineated.

Figure 13 delineates the relationship between temperature and the lattice parameters refined for NPD for PrCe5 and 8YSZ upon cooling in air. With PrCe5 crystallizing in a tetragonal lattice, two distinct linear thermal expansion coefficients, namely α_a for the basal plane and α_c for the c-axis, were obtained. Assuming an even distribution of grain orientation post-electrode manufacturing, the calculated average linear thermal expansion coefficient (TEC) for 8YSZ is estimated at ~ 10.7(1) × 10^{-6} K^{-1} in consistency with published values of 10-11 × 10^{-6} K^{-1}.[43-45] The TEC value for PrCe5 of ~ 13.8(1) × 10^{-6} K^{-1}, lower than the previously reported value of 16.8(2) × 10^{-6} K^{-1} for the Ce-free composition,[46]

places PrCe5 even more closely within the range of common electrolytes such as lanthanum gallate magnesium strontium oxide (LSGM) with TEC of ~ 11-12 × 10^{-6} K^{-1},[47] and GDC with TEC of ~ 12-13 × 10^{-6} K^{-1}.[48,49]

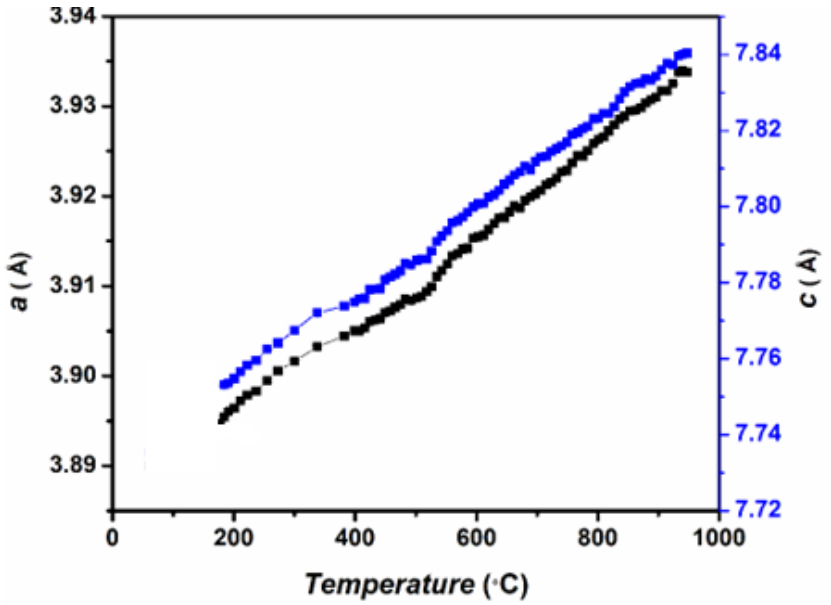

Figure 13. Lattice parameters *a* (in black) and *c* (in blue) for PrCe5, as determined from Neutron Powder Diffraction measurements during cooling in air.

4. Electrochemical performance

The EIS measurements aim to identify the apparent rate-limiting step(s) for hydrogen oxidation, to optimize the operating conditions.[6] The measurements were collected in wet hydrogen atmosphere for electrolyte-supported symmetrical cells on a 250 µm-thick 8YSZ electrolyte. The 8YSZ discs were coated with a dense GDC layer to prevent reaction with Ba-based electrodes. The buffer layer thickness plays a crucial role in electrode performance. A thin GDC layer may fall short in preventing cation diffusion between the electrode and electrolyte, causing stability issues and degradation over time. Conversely, a thick layer provides a superior diffusion barrier, but might impede the flow of ions and electrons, thereby limiting the overall

electrode performance. Therefore, we examined the effects of GDC thicknesses on electrode performance.

4.1 Impact of the GDC thickness on the electrochemical performance

Figure 14 shows Nyquist plots from electrochemical impedance spectroscopy at 750 °C under H_2-3% H_2O, for the PBM, PrCe5, and PrCe5Ni electrodes screen-printed on GDC buffer layers of 1 µm, 3 µm, and 8 µm and sintered in air at 1100 °C for 2 hours. This approach allows for a detailed comparison of the electrochemical properties across different electrode compositions and GDC layer thicknesses.

Focusing specifically on the 1 µm-GDC buffer layer, we examined two samples: PBM and PrCe5. The PrCe5 sample exhibits a slightly smaller impedance, approximately 1.2 Ω cm², compared to the PBM sample, which shows around 1.4 Ω cm². This indicates that there is no noticeable impact of Ce-doping on these samples. Indeed, Ce doping at the *A* site of perovskites may not significantly enhance electrocatalytic properties due to limited redox activity, minimal impact on the electronic structure, and doping concentration limits. The *B* site, typically hosting metals active in redox reactions, plays a more crucial role in determining the electrocatalytic performance of perovskites. The ASR values change over time, as suggested from the slight prolonged "tail" seen in the last data points, which stabilizes around 10 minutes.

Shifting to the 3.5 µm-GDC buffer layer, the three samples, PBM, PrCe5, and PrCe5Ni, revealed interesting trends. The impedance of PBM is reduced, ASR ~ 0.7 Ω cm², in comparison with the 1 µm-GDC case. PrCe5 has a similar impedance to the 1 µm GDC situation, with an ASR ~ 0.9 Ω cm². The addition of nickel to the PrCe5 composition has markedly enhanced its electrical characteristics, reducing the impedance by approximately half when compared to PrCe5. The area-specific resistance (ASR) of PrCe5Ni is around 0.5 Ω cm², notably lower than

the 0.9 Ω cm² measured in PrCe5. The small semicircle at high frequencies for the PrCe5Ni electrode is derived from the charge transfer process. Its low impedance exhibited suggests that the charge transfer processes is efficient, likely due to a combined effect of the improved electrode surface properties by Ce-doping (see paragraph 4.2) and catalytic effect provided by nickel dopant. The larger low frequency semicircle might be associated with surface adsorption/dissociation of H_2 process. Clearly, the presence of Ni (e.g., 3.5 μm GDC case), which is known to be a good catalyst to H-spillover, helps reduce the impedance of this low-frequency process.

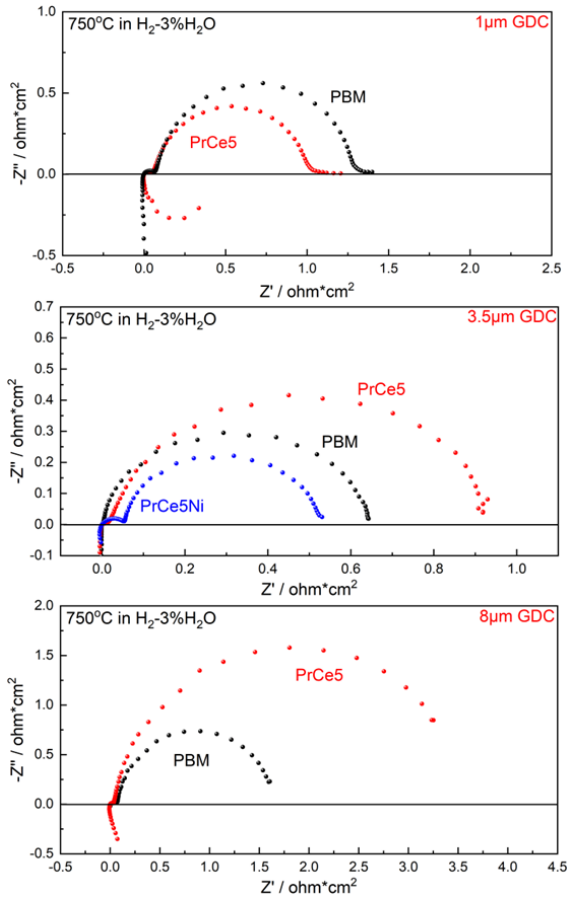

Figure 14. Nyquist plots for electrodes on GDC buffer layer with different thicknesses.

When examining the 8 μm GDC buffer layer, where the PBM and PrCe5 samples were studied, a different behavior is observed. The PrCe5 sample shows a significantly broadened arc than in the 1 μm and 3 μm scenarios. The ASR for PBM is ~ 1.6 Ω cm², while PrCe5 has a remarkably higher value, ASR ~ 3.5 Ω cm². This indicates a substantial variation in electrochemical performance with increased GDC buffer layer thickness, underscoring the complex interplay between material composition and structural dimensions in these systems. The variations in electrochemical performance observed with the 8 μm-GDC buffer layers, particularly the high ASR values for the PrCe5 sample, prompt further investigation into the structural integrity of the cell components. The SEM analysis shown in Figure S4 reveals that the 8 μm-GDC buffer layers, initially well-bonded and uniformly covering the YSZ substrate, experienced peeling, and flaking. This delamination, likely attributable to the thermal expansion coefficient mismatch between GDC and YSZ,[5,50] evidently impacts the stability of the cell and contributes to the observed decrease in electrochemical performance in the thicker GDC buffer layer samples.

4.2 Microstructure analysis for the PBM and PrCe5 electrodes on 3.5 μm-GDC

Figure 15 shows microstructure images of PBM and PrCe5 anodes sintered 3.5 μm-GDC before and after hydrogen testing for 200 h. After testing the PBM electrode exhibits a rougher surface with significant grain growth, increased agglomeration, and reduced porosity, suggesting extensive sintering or material consolidation. In contrast, while the PrCe5 anode also shows grain enlargement and smoothing of particle edges, it maintains more distinct grain boundaries, and appears to experience less agglomeration and reduction in porosity. These morphological alterations indicate that PrCe5 exhibits a more favorable response than PBM to hydrogen

environments, particularly in terms of microstructural evolution and coarsening. This disparity, attributable to cerium doping, may substantially influence the performance of the anodes.

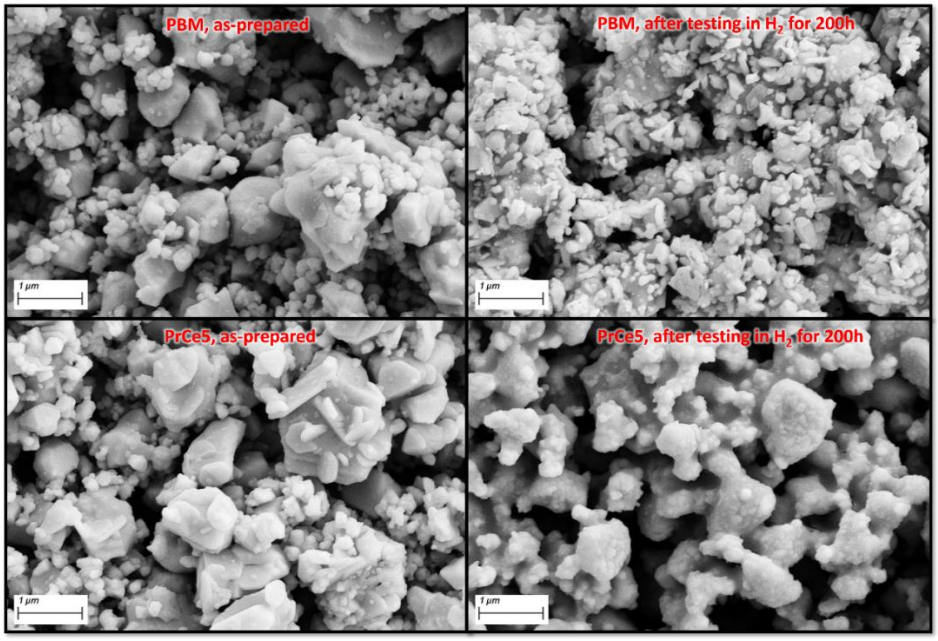

a *b*

Figure 15. SEM images of the PBM and PrCe5 electrodes surfaces (a) before and (b) after hydrogen testing for 200 h revealing morphological changes.

Figures 16 and S5 showcase SEM images alongside EDS barium mapping of the PBM electrode's cross-section, taken before and after hydrogen exposure. These images reveal a modest diffusion of barium through the GDC buffer layer. It is well-established that in electrode materials rich in barium, such as in $Ba_{0.5}Sr_{0.5}Co_{0.8}Fe_{0.2}O_{3-\delta}$, the diffusion of Ba^{2+} ions typically takes place within a temperature spectrum of 850 to 900 ° C.[41,51]

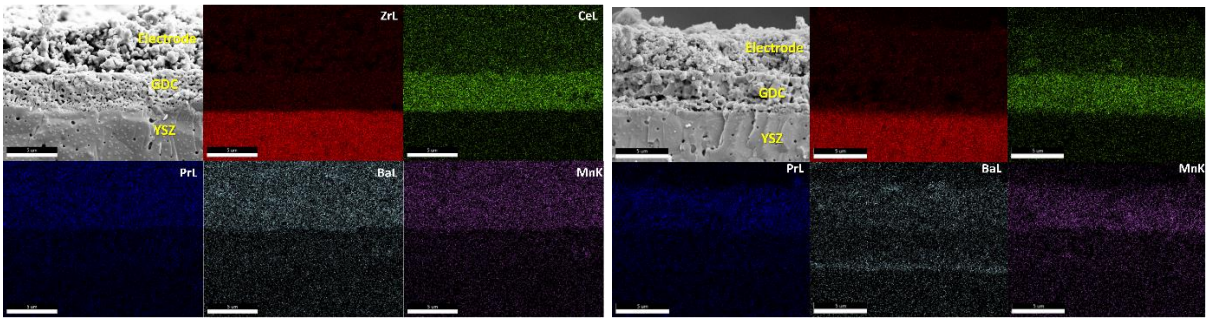

a *b*

Figure 16. Cross-section SEM images and EDS element mapping of the PBM electrode: (a) pre-test baseline and (b) after 200 h of hydrogen exposure demonstrate Ba diffusion across the 3.5 μm GDC buffer layer.

Contrastingly, Figure 17 demonstrates the absence of cation diffusion in the PrCe5 electrode. This comparison implies that while the minor barium migration in the PBM electrode did not affect performance during our 200 hours of hydrogen testing, it might compromise long-term stability. In contrast, the PrCe5 electrode exhibiting no Ba^{2+} diffusion potentially offers enhanced stability under similar conditions. This difference highlights the benefits of cerium doping at minimal levels of 5 at. %, significantly improving the electrode's performance and durability over extended periods.

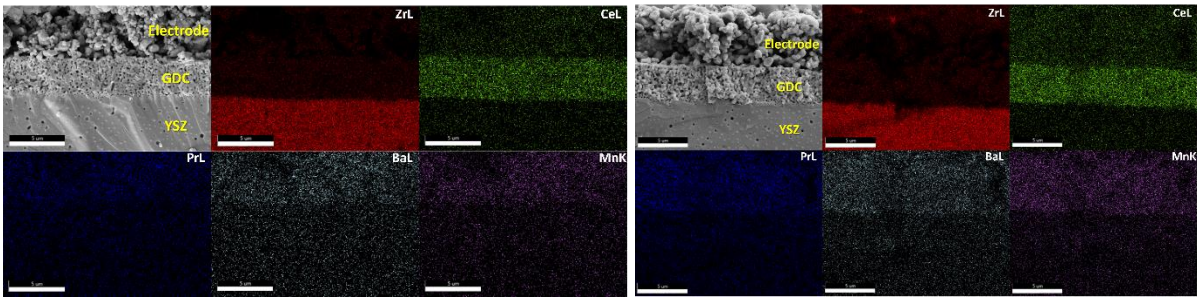

a *b*

Figure 17. Cross-section SEM images and EDS element mapping for PrCe5 electrode: (a) pre-test baseline and (b) after 200 h of hydrogen exposure demonstrate no detectable Ba migration suggesting retention of structural integrity.

The time evolution of the electrochemical performance under H_2 atmospheres for PrCe5/1 µm-GDC and 8 µm-GDC is detailed in the supplementary information, with the corresponding figures illustrated in Figures S6-S10. Figure 18 summarizes the ASR evolution over time for PBM, PrCe5, and PrCeNi electrodes under H_2 at 750 °C, across GDC buffer layers of 1 µm, 3.5 µm, and 8 µm. With 1 µm GDC, PBM and PrCe5 experience a rapid R_p increase, estimated at 0.15-0.2 Ω cm^2 h^{-1}. At 3.5 µm, all electrodes maintain stable R_p values, with an estimated increase of ~ 0.002 Ω cm^2 h^{-1}. With 8 µm, PBM shows moderate ASR increases, while PrCe5 remains stable. Those results suggest a 3.5 µm GDC layer as optimal for praseodymium barium double perovskite manganite electrodes in SOFC anodes, differing from previous studies of Briois *et al*. recommending ~ 0.57 µm. [52] The 3.5 µm GDC layer thickness achieves the lowest ASR after 220 hours at T = 750 °C for our Ba-rich double layered perovskite anodes in a

hydrogen environment, supporting the effectiveness of 2-4 µm GDC layers for SOFC anode performance and mass production.[53]

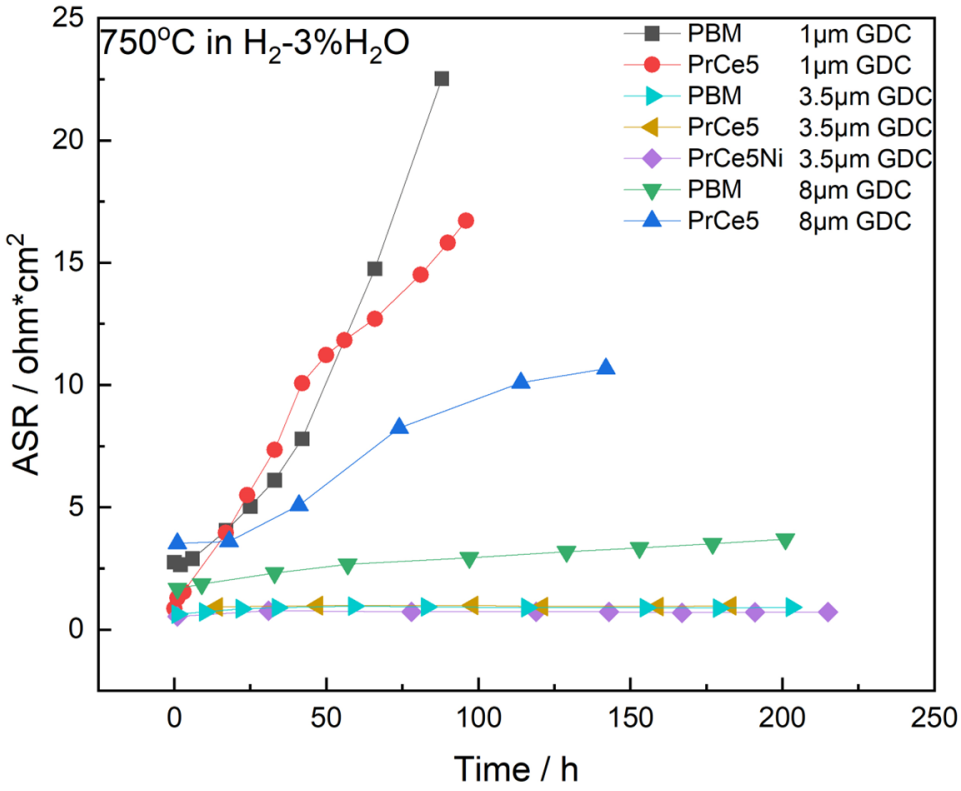

Figure 18. Area Specific Resistance (ASR) as a function of time for PBM, PrCe5 and PrCe5Ni anodes at 750 °C in H_2-3% H_2O with varying GDC buffer layer thicknesses.

Conclusion

Our study has explored the impact of cerium and nickel doping on the performance of $PrBaMn_2O_5$ anodes in a wet hydrogen atmosphere. The interaction between the doped electrodes and the YSZ electrolyte was monitored through high-temperature neutron diffraction techniques up to 950 °C, highlighting the critical role of GDC buffer layer thickness in preserving electrode-electrolyte interface stability. Incorporating 5% cerium into PrCe5 anodes results in superior microstructural stability and reduced particle agglomeration compared to PBM when exposed to hydrogen, hinting improved performance and longevity. Moreover, unlike PBM, PrCe5 shows no signs of barium diffusion, indicating that cerium doping plays a crucial role in preserving the electrode's structural integrity over extended periods. Further

research will also examine the anode's performance in an H_2-H_2S atmosphere to assess its sulfur tolerance and in hydrocarbon fuels to evaluate its coking resistance, a key factor for practical SOFC deployment. This ongoing research is expected to contribute substantially to enhancing the efficiency, and longevity of SOFC technology.

Acknowledgements

This research received critical support from the Ministry for Higher Education, Research, and Innovation (MESRI), which provided a Ph.D. grant to P.M. Furthermore, M.B. expresses her gratefulness to the Institute Laue-Langevin (ILL) for generously allocating beam time for our experiments, as well as to A. Daramsy for his invaluable technical assistance. We would also like to extend our appreciation to L. Joanny of the CMEBA facility at ScanMAT, University of Rennes, for his contributions in conducting scanning electron microscopy (SEM) measurements. Furthermore, our sincere thanks go to S. Ollivier for her invaluable assistance in performing hydrogen reduction experiments. We acknowledge the financial support provided to M.B. through State aid, administered by the National Research Agency, the principal operator of the France 2030 program (ANR-22-PEHY-0003). YW and KH would also like to thank the supports from U.S. Department of Energy's Office of Energy Efficiency and Renewable Energy (EERE), the Fuel Cell Technologies Office (FCTO) under Award Number DE-EE-0008842 and Office of Fossil Energy and Carbon Management under National Energy Technology Lab under award number DE-FE-32111.

References

(1) Ruiz-Morales, J. C.; Canales-Vázquez, J.; Ballesteros-Pérez, B.; Peña-Martínez, J.; Marrero-López, D.; Irvine, J. T. S.; Núñez, P. LSCM–(YSZ–CGO) composites as improved symmetrical electrodes for solid oxide fuel cells. *Journal of the European Ceramic Society* **2007,** *27* (13), 4223.
(2) Deleebeeck, L.; Fournier, J. L.; Birss, V. Comparison of Sr-doped and Sr-free La1−xSrxMn0.5Cr0.5O3±δ SOFC Anodes. *Solid State Ionics* **2010,** *181* (25), 1229.
(3) Ormerod, R. M. Solid oxide fuel cells. *Chemical Society Reviews* **2003,** *32* (1), 17.
(4) Minh, N. Q. Solid oxide fuel cell technology—features and applications. *Solid State Ionics* **2004,** *174* (1), 271.
(5) Huang, K.; Goodenough, J. B. In *Solid Oxide Fuel Cell Technology*; Huang, K.;Goodenough, J. B., Eds.; Woodhead Publishing, 2009, DOI:https://doi.org/10.1533/9781845696511.156 https://doi.org/10.1533/9781845696511.156.
(6) Huang, K.; Goodenough, J. B. *Solid Oxide Fuel Cell Technology: Principles, Performance And Operations*; Woodhead Publishing, 2009.
(7) Huang, K.; Lee, H. Y.; Goodenough, J. B. Sr- and Ni-Doped LaCoO3 and LaFeO3 Perovskites: New Cathode Materials for Solid-Oxide Fuel Cells. *Journal of The Electrochemical Society* **1998,** *145* (9), 3220.
(8) Hubert, M.; Laurencin, J.; Cloetens, P.; MOREL, B.; Montinaro, D.; Lefebvre-Joud, F. Impact of Nickel Agglomeration on Solid Oxide Cell Operated in Fuel Cell and Electrolysis Modes. *Journal of Power Sources* **2018**.
(9) Mogensen, M. B.; Hauch, A.; Sun, X.; Chen, M.; Tao, Y.; Ebbesen, S. D.; Hansen, K. V.; Hendriksen, P. V. Relation Between Ni Particle Shape Change and Ni Migration in Ni–YSZ Electrodes – a Hypothesis. *Fuel Cells* **2017,** *17* (4), 434.
(10) Fuerte, A.; Valenzuela, R. X.; Escudero, M. J.; Daza, L. Effect of cobalt incorporation in copper-ceria based anodes for hydrocarbon utilisation in Intermediate Temperature Solid Oxide Fuel Cells. *Journal of Power Sources* **2011,** *196* (9), 4324.
(11) Sfeir, J.; Buffat, P. A.; Möckli, P.; Xanthopoulos, N.; Vasquez, R.; Joerg Mathieu, H.; Van herle, J.; Ravindranathan Thampi, K. Lanthanum Chromite Based Catalysts for Oxidation of Methane Directly on SOFC Anodes. *Journal of Catalysis* **2001,** *202* (2), 229.
(12) Atkinson, A.; Barnett, S.; Gorte, R. J.; Irvine, J. T. S.; McEvoy, A. J.; Mogensen, M.; Singhal, S. C.; Vohs, J. In *Materials for Sustainable Energy*; Co-Published with Macmillan Publishers Ltd, UK, 2010, DOI:doi:10.1142/9789814317665_0030
(13) Skinner, S. J.; Packer, R. J.; Bayliss, R. D.; Illy, B.; Prestipino, C.; Ryan, M. P. Redox chemistry of the novel fast oxide ion conductor CeNbO4 + d determined through an in-situ spectroscopic technique. *Solid State Ionics* **2011,** *In Press, Corrected Proof*.
(14) Lay, E.; Benamira, M.; Pirovano, C.; Gauthier, G.; Dessemond, L. Effect of Ce-Doping on the Electrical and Electrocatalytical Behavior of La/Sr Chromo-Manganite Perovskite as New SOFC Anode. *Fuel Cells* **2012,** *12* (2), 265.
(15) Lay, E.; Dessemond, L.; Gauthier, G. Synthesis and Characterization of CexSr1-xCr0.5Mn0.5O3-δ Perovskites as Anode Materials for Solid Oxide Fuel Cells (SOFC). *Electrochimica Acta*, DOI:http://dx.doi.org/10.1016/j.electacta.2016.09.044
(16) Ran, R.; Wu, X. D.; Quan, C. Z.; Weng, D. Effect of strontium and cerium doping on the structural and catalytic properties of PrMnO₃ oxides. *SOLID STATE IONICS* **2005,** *176* (9-10), 965.
(17) Zhou, X.-W.; Sun, Y.-F.; Wang, G.-Y.; Gao, T.; Chuang, K. T.; Luo, J.-L.; Chen, M.; Birss, V. I. Synthesis and electrocatalytic performance of La0.3Ce0.1Sr0.5Ba0.1TiO3 anode catalyst for solid oxide fuel cells. *Electrochemistry Communications* **2014,** *43*, 79.
(18) Périllat-Merceroz, C.; Gauthier, G.; Roussel, P.; Huvé, M.; Gélin, P.; Vannier, R.-N. Synthesis and Study of a Ce-Doped La/Sr Titanate for Solid Oxide Fuel Cell Anode Operating Directly on Methane. *Chemistry of Materials* **2011,** *23* (6), 1539.
(19) Shen, J.; Yang, G.; Zhang, Z.; Zhou, W.; Wang, W.; Shao, Z. Tuning layer-structured La0.6Sr1.4MnO4+δ into a promising electrode for intermediate-temperature symmetrical

solid oxide fuel cells through surface modification. *Journal of Materials Chemistry A* **2016,** *4* (27), 10641.

(20) Jiang, S. P. A review of wet impregnation—An alternative method for the fabrication of high performance and nano-structured electrodes of solid oxide fuel cells. *Materials Science and Engineering: A* **2006,** *418* (1), 199.

(21) Bahout, M.; Managutti, P. B.; Dorcet, V.; Le Gal La Salle, A.; Paofai, S.; Hansen, T. C. In situ exsolution of Ni particles on the PrBaMn2O5 SOFC electrode material monitored by high temperature neutron powder diffraction under hydrogen. *Journal of Materials Chemistry A* **2020,** *8* (7), 3590.

(22) Kwon, O.; Sengodan, S.; Kim, K.; Kim, G.; Jeong, H. Y.; Shin, J.; Ju, Y.-W.; Han, J. W.; Kim, G. Exsolution trends and co-segregation aspects of self-grown catalyst nanoparticles in perovskites. *Nature Communications* **2017,** *8*, 15967.

(23) Gu, Y.; Zhang, Y.; Zheng, Y.; Chen, H.; Ge, L.; Guo, L. PrBaMn2O5+δ with praseodymium oxide nano-catalyst as electrode for symmetrical solid oxide fuel cells. *Applied Catalysis B: Environmental* **2019,** *257*, 117868.

(24) Tsoga, A.; Naoumidis, A.; Stöver, D. Total electrical conductivity and defect structure of ZrO2–CeO2–Y2O3–Gd2O3 solid solutions. *Solid State Ionics* **2000,** *135* (1), 403.

(25) Xu, G.; Ma, H.; Zhong, M.; Zhou, J.; Yue, Y.; He, Z. Influence of pH on characteristics of BaFe12O19 powder prepared by sol–gel auto-combustion. *Journal of Magnetism and Magnetic Materials* **2006,** *301* (2), 383.

(26) Roisnel, T.; Rodriguez-Carvajal, J. In *Epdic 7: European Powder Diffraction, Pts 1 and 2*; Delhez, R.;Mittemeijer, E. J., Eds., 2001; Vol. 378-3.

(27) Hansen, T. C.; Henry, P. F.; Fischer, H. E.; Torregrossa, J.; Convert, P. The D20 instrument at the ILL: a versatile high-intensity two-axis neutron diffractometer. *Measurement Science and Technology* **2008,** *19* (3), 034001.

(28) Tonus, F.; Bahout, M.; Battle, P. D.; Hansen, T.; Henry, P. F.; Roisnel, T. In situ neutron diffraction study of the high-temperature redox chemistry of Ln(3-x)Sr(1+x)CrNiO(8-delta) (Ln = La, Nd) under hydrogen. *Journal of Materials Chemistry* **2010,** *20* (20), 4103.

(29) Managutti, P. B.; Yu, H.; Hernandez, O.; Prestipino, C.; Dorcet, V.; Wang, H.; Hansen, T. C.; Bahout, M. Exsolution of Co–Fe Alloy Nanoparticles on the PrBaFeCoO5+δ Layered Perovskite Monitored by Neutron Powder Diffraction and Catalytic Effect on Dry Reforming of Methane. *ACS Applied Materials & Interfaces* **2023,** *15* (19), 23040.

(30) Managutti, P. B.; Tymen, S.; Liu, X.; Hernandez, O.; Prestipino, C.; Le Gal La Salle, A.; Paul, S.; Jalowiecki-Duhamel, L.; Dorcet, V.; Billard, A.et al. Exsolution of Ni Nanoparticles from A-Site-Deficient Layered Double Perovskites for Dry Reforming of Methane and as an Anode Material for a Solid Oxide Fuel Cell. *ACS Applied Materials & Interfaces* **2021,** *13* (30), 35719.

(31) Rodríguez-Carvajal, J. Recent advances in magnetic structure determination by neutron powder diffraction. *Physica B: Condensed Matter* **1993,** *192* (1-2), 55.

(32) Bérar, J. F.; Lelann, P. E.s.d.'s and estimated probable error obtained in Rietveld refinements with local correlations. *Journal of Applied Crystallography* **1991,** *24* (1), 1.

(33) Briois, V.; Fonda, E.; Belin, S.; Barthe, L.; La Fontaine, C.; Langlois, F.; Ribbens, M.; Villain, F. SAMBA: The 4–40 keV X-ray absorption spectroscopy beamline at SOLEIL. *UVX 2010 - 10e Colloque sur les Sources Cohérentes et Incohérentes UV, VUV et X ; Applications et Développements Récents* **2011**, 41.

(34) Breaz, E.; Aubry, E.; Billard, A.; Coton, N.; Coquoz, P.; Pappas, A.; Diethelm, S.; Ihringer, R.; Briois, P. Influence of the Bias Substrate Power on the GDC Buffer Layer. *ECS Transactions* **2017,** *78* (1), 807.

(35) Tsoga, A.; Gupta, A.; Naoumidis, A.; Nikolopoulos, P. Gadolinia-doped ceria and yttria stabilized zirconia interfaces: regarding their application for SOFC technology. *Acta Materialia* **2000,** *48* (18), 4709.

(36) Shannon, R. D. Revised effective ionic radii and systematic studies of interatomic distances in halides and chalcogenides. *Acta Crystallographica Section A* **1976,** *32* (5), 751.

(37) Bahout, M.; Pramana, S. S.; Hanlon, J. M.; Dorcet, V.; Smith, R. I.; Paofai, S.; Skinner, S. J. Stability of NdBaCo2-xMnxO5+[small delta] (x = 0, 0.5) layered perovskites under humid conditions investigated by high-temperature in situ neutron powder diffraction. *Journal of Materials Chemistry A* **2015,** *3* (30), 15420.

(38) Faes, A.; Hessler-Wyser, A.; Zryd, A.; Van herle, J. A Review of RedOx Cycling of Solid Oxide Fuel Cells Anode. *Membranes* **2012,** *2* (3), 585.

(39) Sun, Y.-F.; Zhou, X.-W.; Zeng, Y.; Amirkhiz, B. S.; Wang, M.-N.; Zhang, L.-Z.; Hua, B.; Li, J.; Li, J.-H.; Luo, J.-L. An ingenious Ni/Ce co-doped titanate based perovskite as a coking-tolerant anode material for direct hydrocarbon solid oxide fuel cells. *Journal of Materials Chemistry A* **2015,** *3* (45), 22830.

(40) Castillo-Martínez, E.; Williams, A. J.; Attfield, J. P. High-temperature neutron diffraction study of the cation ordered perovskites TbBaMn2O5+x and TbBaMn2O5.5−y. *Journal of Solid State Chemistry* **2006,** *179* (11), 3505.

(41) Duan, Z.; Yang, M.; Yan, A.; Hou, Z.; Dong, Y.; Chong, Y.; Cheng, M.; Yang, W. Ba0.5Sr0.5Co0.8Fe0.2O3−δ as a cathode for IT-SOFCs with a GDC interlayer. *Journal of Power Sources* **2006,** *160* (1), 57.

(42) Kim, Y.-M.; Kim-Lohsoontorn, P.; Bae, J. Effect of unsintered gadolinium-doped ceria buffer layer on performance of metal-supported solid oxide fuel cells using unsintered barium strontium cobalt ferrite cathode. *Journal of Power Sources* **2010,** *195* (19), 6420.

(43) Hayashi, H.; Saitou, T.; Maruyama, N.; Inaba, H.; Kawamura, K.; Mori, M. Thermal expansion coefficient of yttria stabilized zirconia for various yttria contents. *Solid State Ionics* **2005,** *176* (5–6), 613.

(44) Tietz, F. Thermal expansion of SOFC materials. *Ionics* **1999,** *5* (1), 129.

(45) Zhang, S.-L.; Wang, H.; Lu, M. Y.; Zhang, A.-P.; Mogni, L. V.; Liu, Q.; Li, C.-X.; Li, C.-J.; Barnett, S. A. Cobalt-substituted SrTi0.3Fe0.7O3−δ: a stable high-performance oxygen electrode material for intermediate-temperature solid oxide electrochemical cells. *Energy & Environmental Science* **2018,** *11* (7), 1870.

(46) Sengodan, S.; Choi, S.; Jun, A.; Shin, T. H.; Ju, Y.-W.; Jeong, H. Y.; Shin, J.; Irvine, J. T. S.; Kim, G. Layered oxygen-deficient double perovskite as an efficient and stable anode for direct hydrocarbon solid oxide fuel cells. *Nat Mater* **2015,** *14* (2), 205.

(47) Naiqing, Z.; Kening, S.; Derui, Z.; Dechang, J. Study on Properties of LSGM Electrolyte Made by Tape Casting Method and Applications in SOFC. *Journal of Rare Earths* **2006,** *24* (1, Supplement 1), 90.

(48) Tompsett, G. A.; Sammes, N. M.; Yamamoto, O. Ceria–Yttria-Stabilized Zirconia Composite Ceramic Systems for Applications as Low-Temperature Electrolytes. *Journal of the American Ceramic Society* **1997,** *80* (12), 3181.

(49) Hayashi, H.; Kanoh, M.; Quan, C. J.; Inaba, H.; Wang, S.; Dokiya, M.; Tagawa, H. Thermal expansion of Gd-doped ceria and reduced ceria. *Solid State Ionics* **2000,** *132* (3–4), 227.

(50) Hussain, S.; Yangping, L. Review of solid oxide fuel cell materials: cathode, anode, and electrolyte. *Energy Transitions* **2020,** *4* (2), 113.

(51) Qingshan, Z.; Tongan, J.; Yong, W. Thermal expansion behavior and chemical compatibility of BaxSr1−xCo1−yFeyO3−δ with 8YSZ and 20GDC. *Solid State Ionics* **2006,** *177* (13), 1199.

(52) Bouleau, L.; Coton, N.; Coquoz, P.; Ihringer, R.; Billard, A.; Briois, P. GDC Buffer Layer Synthesized by Reactive Magnetron Sputtering: Effect of Total Pressure and Thickness on SOFC Performances. *Crystals* **2020,** *10* (9), 759.

(53) Hussain, A.; Song, R.-H.; Khan, M. Z.; Kim, T.-H.; Hong, J.-E.; Joh, D. W.; Ishfaq, H. A.; Lee, S.-B.; Lim, T.-H. Durability improvement of large-area anode supported solid oxide fuel cell fabricated by 4-layer sequential co-lamination and co-firing process. *Journal of Power Sources* **2023,** *573*, 233160.